Arabian Journal of Chemistry (2023) 16, 104963

King Saud University

Arabian Journal of Chemistry

www.ksu.edu.sa
www.sciencedirect.com

ORIGINAL ARTICLE

Electrochemical determination of imatinib mesylate using $TbFeO_3/g\text{-}C_3N_4$ nanocomposite modified glassy carbon electrode

Mahin Baladi [a], **Hakimeh Teymourinia** [b,c], **Elmuez A. Dawi** [d], **Mahnaz Amiri** [e,f], **Ali Ramazani** [b,c,*], **Masoud Salavati-Niasari** [a,*]

[a] *Institute of Nano Science and Nano Technology, University of Kashan, P.O. Box 87317-51167, Kashan, Iran*
[b] *Department of Biotechnology, Research Institute of Modern Biological Techniques (RIMBT), University of Zanjan, P.O. Box 45371-38791, Zanjan, Iran*
[c] *Department of Chemistry, Faculty of Science, University of Zanjan, P.O. Box 45371-38791, Zanjan, Iran*
[d] *Nonlinear Dynamic Research Center (NDRC), College of Humanities and Sciences, Ajman University, P.O. Box 346, Ajman, United Arab Emirates*
[e] *Neuroscience Research Center, Institute of Neuropharmacology, Kerman University of Medical Science, Kerman, Iran*
[f] *Department of Hematology and Laboratory Sciences, Faculty of Allied Medical Sciences, Kerman University of Medical Sciences, Kerman, Iran*

Received 7 February 2023; revised 13 April 2023; accepted 26 April 2023
Available online 3 May 2023

KEYWORDS

Imatinib Mesylate;
$TbFeO_3/g\text{-}C_3N_4$ Nanocomposite;
Electrochemical Determination;
Electrochemical Sensor;
Nanostructures

Abstract A new electrochemical sensor based on a glassy carbon electrode (GCE) modified by Tb (Terbium) $FeO_3/g\text{-}C_3N_4$ (graphitic carbon nitride) nanocomposite has been developed. In order to characterize the nanocomposite produced, several techniques were employed, including X-ray diffraction (XRD), Fourier transform infrared, Field Emission Scanning Electron Microscope, Energy Dispersive X-ray Spectroscopy, Brunauer-Emmett-Teller, vibrating sample magnetometry, and Transmission Electron Microscopy (TEM). According to XRD data, the nanocomposite produced contained particles of about 36 ± 2 nm in size. TEM examination of the voltammetric response of the offered sensor ($TbFeO_3/g\text{-}C_3N_4$ nanocomposite/glassy carbon electrode (GCE)) demonstrated a catalytic effect against imatinib. In optimized solution pH and scan rate conditions, this sensor demonstrated an excellent electrocatalytic response for detecting imatinib. Furthermore,

---

[*] Corresponding authors at: Department of Biotechnology, Research Institute of Modern Biological Techniques (RIMBT), University of Zanjan, P.O. Box 45371-38791, Zanjan, Iran (A. Ramazani).
E-mail addresses: aliramazani@gmail.com (A. Ramazani), salavati@kashanu.ac.ir (M. Salavati-Niasari).

Peer review under responsibility of King Saud University. Production and hosting by Elsevier.

ELSEVIER | Production and hosting by Elsevier

https://doi.org/10.1016/j.arabjc.2023.104963

the fabricated sensor demonstrated acceptable accuracy, reproducible behavior, and a high level of stability during all electrochemical tests. In addition, analytical parameters were determined and the results were compared with those from previous studies.

1. Introduction

Imatinib mesylate (IMAT) is a particular drug with the molecular formula of 4-[(4-methylpiperazin-1-yl) methyl]-N- [4-methyl-3-[(4-pyridin-3-ylpyrimidin-2-yl) amino] phenyl]benzamide that is used to treat chronic myeloid leukemia (CML) and diseases such as gastrointestinal stromal tumors (Druker et al., 2001, Gibbons et al., 2008). Imatinib mesylate significantly alters the management of tumors that are resistant to cytotoxic chemotherapy by inhibiting tyrosine kinase (Hunter 2007). CML, is a malignant blood disorder in which the arms of chromosomes 9 and 22 are displaced causes abnormal proliferation of myeloid cells, leading to the production of the BCR-ABL fusion protein, which encodes a protein with high tyrosine kinase activity (Mauro and Deininger 2006, Nabi et al., 2021, Mohaghegh et al., 2022). IMAT is mostly metabolized by the enzyme CYP3A4 (Deininger and Druker 2003). Depending on the dose of this drug, patients can have very diverse circulating concentrations, which illustrates the importance of plasma IMAT concentrations for patients' clinical outcomes (Larson et al., 2008). It is therefore essential to measure the concentration of IMAT in plasma in order to control CML disease (Ajimura et al., 2011, Rahimi Kakavandi et al., 2021). Several instrumental methods, such as high-performance liquid chromatography-ultraviolet detection (HPLC/UV) have been reported in the literature. (Hasin et al., 2017), gas chromatography (Karim et al., 2012), HPLC/mass spectrometry detection (Andriamanana et al., 2013), spectrophotometric methods (Karim et al., 2014), capillary electrophoresis (Rodríguez-Flores et al., 2005) and electrochemical methods (Rodriguez et al., 2005, Hatamluyi and Es' haghi 2017, Rodríguez et al., 2018, Ghapanvari et al., 2020, Rezvani Jalal et al., 2020, Wu et al., 2021, Gondo 2022) have been used to measure IMAT drug in blood plasma and other biological samples. Although some of these techniques possess a high degree of sensitivity and selectivity, there are some limitations, including long analysis times, expensive tools, well-equipped laboratories, problematic sample preparation steps, difficult operations, and the need for skilled and trained personnel. Due to some advantages, electrochemical diagnostic methods have been considered more frequently than the methods mentioned due to the fact that they offer a high degree of sensitivity and selectivity, do not require sophisticated instruments, require a shorter analysis time, and are easier to apply (Yousefi et al., 2011, Teymourinia et al., 2020, Amiri and Mahmoudi-Moghaddam 2021, Ghalkhani et al., 2022, Sohouli et al., 2022, Sohouli et al., 2022, Bobinov et al., 2021).

In the manufacture of electrochemical sensors, the selection of appropriate nanomaterials with high selectivity, sensitivity, and stability is the primary challenge (Farvardin et al., 2020, Iranmanesh et al., 2020, Zhang et al., 2020, Moarefdoust et al., 2021, Abbasi et al., 2023, Foroughi and Jahani 2022, Jahani et al., 2022, Ghasemi et al., 2023, Taherizadeh et al., 2023). Sensors for detecting diverse analytes in diverse biological and environmental fluids can be fabricated using a variety of materials, including polymers, carbon nanomaterials, and metal oxide nanoparticles (Halali et al., 2020, Tajik et al., 2021, Terán-Alcocer et al., 2021, Abdulhusain et al., 2022, Mahde et al., 2022, Al-Alwany, 2022). Graphitic carbon nitride ($g\text{-}C_3N_4$) has recently gained more attention than other nanomaterials due to its properties such as ease of fabrication, low cost, high thermal, chemical, and mechanical stability, as well as its unique structure. A graphitic structure of $g\text{-}C_3N_4$ containing nitrogen atoms and SP2 hybridization provides more surface-active sites for adsorption of compounds (Wang et al., 2020). As a result of the graphitic layer structure of this material, a series of weak interactions between the carbon and nitrogen layers can be achieved to form very thin structural plates for use in electrochemical sensors. The thin and high-area layers enable rapid transfer of the carrier from the inside to the surface. Although $g\text{-}C_3N_4$ nanostructures have unique characteristics, they are not suitable for electrochemical analysis due to their low electrical conductivity (Hassannezhad et al., 2019). Recent research has focused on the study of ABO_3-type oxide perovskites (where the A-site cation is usually occupied by an alkaline-earth or rare-earth metal, while the B-site cation is typically occupied by a transition metal cation) because they possess certain properties. The latter, such as high structural porosity, simple synthesis, thermal stability, high surface area, the ability to change the structure and form hybrids with other structures, high ionic and electronic conductivity, short electron transfer pathway, enhanced catalytic activity, special electrical properties, and significant optical potentials (Warshi et al., 2018, Salavati-Niasari et al., 2004, Teymourinia et al., 2020, Salavati-Niasari et al., 2009). For the analysis of environmental pollutants by different electrochemical methods, the use of ABO_3 type perovskite-based electrode modifiers has resulted in good analytical results, including a wide linear range, good detection limits, high selectivity, accuracy and reproducibility (Warshi et al., 2018). Many studies have been conducted on the use of perovskite materials such as $LaFeO_3$, $LaCoO_3$, and $NdFeO_3$ to modify electrodes for the measurement of pharmaceuticals and biological compounds such as dopamine, uric acid, ascorbic acid, catechol, and flutamide (Atta et al., 2019). Rare earth orthoferrites like $RFeO_3$ (R ion states rare-earth ions) have recently been considered because of their innovative magnetic and electrical properties, such as controllable magnetic properties by altering the electric field and practical temperature, spin orientation capability, and photocatalytic and magneto-optical effects (Vijayaraghavan et al., 2017, Anajafi et al., 2019, Salavati-Niasari and Amiri, 2005). Research has shown that the replacement of transition elements with Fe, a metal oxide with adjustable spin and oxidation states, plays an important role in the chemical, magnetic, and electrical properties of $RFeO_3$-based metal oxides (Zhang et al., 2017). The synthesis of nanoparticles can be classified into three categories, namely chemical, physical, and biological. By far the simplest, non-toxic, and most economical method of synthesizing nanoparticles is biological synthesis. A significant role is played by surface coatings and reducing agents during the synthesis of nanoparticles. In the physical and chemical methods of synthesis of nanoparticles, toxic and dangerous substances are used, which cause defects in nature. The cost of surface covering agents and reducing agents is high, and therefore it is not economically feasible to synthesize these materials. Accordingly, the green method is the most effective method for preparing nanoparticles. The most famous species of the genus Diospyros is Diospyros kaki. L (Oriental persimmon). D. For more than 2000 years, kaki has been cultivated in China and consumed as a food. One of the main macronutrients found in Diospyros kaki. L fruit is carbohydrates. In terms of energy, this fruit has nearly 76.60 kcal per 100 g^{-1}, of which 75.33 kcal come from. The majority of carbohydrates in persimmons are monosaccharides and disaccharides, including glucose, fructose, and sucrose, which have a mean of 7.41, 5.96, and 1.06 g per 100 g of fresh fruitage, respectively (Matheus et al., 2022). For the first time, we synthesized $TbFeO_3$ nanoparticles using the fruit extract Diospyros kaki. L as a natural fuel. Dual composites containing carbon-based nanomaterials ($g\text{-}C_3N_4$) and $RFeO_3$-based novel metal oxide perovskites can overcome the low conductivity of $g\text{-}C_3N_4$ through synergistic effects. In our knowledge, there have been very few studies conducted on electrochemical analysis of the IMAT drug. The present study is the first to use a composite consisting of g-C_3N_4 and $TbFeO_3$ to improve the surface of glassy carbon electrodes (GCEs). A layered or two-dimensional structure of g-C_3N_4 is one of the most stable forms under ambient conditions. The graphitic planes are interconnected with amino groups called tri-s-triazine units. Using these units, carbon nitride polymers can be synthesized that exhibit a variety of electronic properties. A major step in the fabrication of electrochemical sensors involves the immobilization of nanocomposite materials of carbon and perovskites on the electrode surface. Different substrate materials can be loaded to produce new electrodes with recognition capabilities. Therefore, in this study, we have developed a modified GCE based on $TbFeO_3$/g-C_3N_4 nanocomposite for the determination of IMAT drugs. The electrode has been modified to demonstrate remarkable electrocatalytic activity for the detection of IMAT in biological samples with reasonable analytical results.

2. Experimental

2.1. Materials and methods

Merck provided the chemicals used in the preparation of samples, including terbium (III) nitrate pentahydrate, iron (III) nitrate nonahydrate, and melamine. We used the material as received without further purification. Crystallinity, sample composition, and phase determination were determined using Fourier transform infrared spectroscopy (FT-IR; Nicolet M. agna-550 spectrophotometer) and X-ray diffraction (XRD; Philips). Irradiation of copper with nickel ($\lambda = 1.54$ Å); scan range $10 < 2\theta < 80$). FE-SEM (Field Emission Scanning Electron Microscope) (Mira3 Tescan) and TEM (Transmission Electron Microscope) (HT-7700) were used to examine the surface characteristics and morphology of samples. An EDS (Energy Dispersive Spectrometry) analysis was conducted using a Philips XL30 microscope. Moreover, the magnetic properties were measured using a VSM (vibrating sample magnetometer) (Desert Precision Magnetism Company, Kashan Kavir, and Iran). N_2 adsorption/desorption analysis (BET) was conducted at 195 °C using an automatic gas adsorption analyzer (Tristar 3000, Micromeritics) to determine the size and type of nanoparticle pores.

2.2. Extract preparation of Diospyros kaki.L

To extract Diospyros kaki L., about 300 g of fresh persimmon fruit were washed well and extracted using acetone: water (80:20 volume/volume). Afterwards, it is homogenized at room temperature on a mechanical stirrer for 30 min. A 10-minute centrifugation was performed on the extracted extract. Afterwards, the supernatant was collected and filtered with Whatman paper, and the extract obtained was dried in the oven and stored in the refrigerator.

2.3. Synthesis of pure $TbFeO_3$

A green sol–gel combustion method was used in this experiment to prepare $TbFeO_3$ nanostructures. As a first step, 1 mmol (0.1 g) of $Tb(NO_3)_3{\cdot}5H_2O$ and 1 mmol (0.092 g) of $Fe(NO_3)_2{\cdot}9H_2O$ are dissolved in 15 ml of distilled water. As a fuel, 0.2 g of diospyros kaki. L extract was added to the solution obtained in the previous step. We placed the solution under a temperature of 80 °C for 30 min. Upon reaching 150 °C, the viscous solution evaporated and transformed into ashes. The powder obtained after drying was placed in an oven at 80 °C for one day in order to complete the drying process. Lastly, the obtained product was calcined at 800 °C for four hours. There are carbohydrates present in Diospyros kaki. L fruit (including glucose, fructose, and sucrose) that are used as fuel. A fuel with appropriate ligand strength, metal ion protection by surface active complex, and different combustion temperatures due to carbon bulk suggest different properties of $TbFeO_3$ nanostructures.

2.4. Fabrication of g-C_3N_4 and $TbFeO_3$/g-C_3N_4 nanocomposites

In order to prepare g-C_3N_4, two grams of melamine were heated to 550 °C for four hours, and the obtained yellow powder was collected for further investigation. Afterwards, 0.45 g of g-C_3N_4 in 50 ml of water was subjected to sonication for 5 min and the mixture was stirred for 2 h in order to prepare the nanocomposite. After stirring for 30 min, 0.45 g of $TbFeO_3$ nanostructure was added to this suspension. After centrifugation and washing with ethanol and water several times, the nanocomposites were dried at 75 °C for one day (Scheme 1).

2.5. Preparation of sensor

An electrochemical sensor was initially prepared by cleaning the GCE with alumina powder and washing it with water and acetone. After synthesizing the nanocomposite, it was dispersed in 1 mg of ethanol and 2 μL of it was placed on the electrode surface and dried at 50 °C. This electrode was referred to as $TbFeO_3$/g-C_3N_4/GCE. The same procedure was followed for the preparation of g-C_3N_4/GCE.

3. Result and discussions

3.1. X-ray diffraction analysis

Fig.S1 illustrates the XRD patterns of (a) graphite carbon nitride and (b) $TbFeO_3$ nanoparticles prepared with diospyros kaki.L extract at 800 °C for four hours. Based on the XRD pattern of g-C_3N_4 and the significant diffraction peak at $2\theta = 27.2°$, this can be attributed to the (002) facet of Graphite Carbon Nitride. Several diffraction peaks of pure $TbFeO_3$ have been observed at 21.1°, 23.01°, 26.2°, 32.18°, 33.06°, 34°, 40.03°, and 59.4°, which correspond to (112), (202), (123), (200), (301), (115) and (004) crystal planes of $TbFeO_3$ perovskite nanostructures with reference code (47–0068). Therefore, it confirms that $TbFeO_3$ nanostructures produced by the combustion method have a high degree of crystallinity. A heterojunction $TbFeO_3$/g-C_3N_4 nanocomposites sample shown in Fig. 1 retained the characteristics of pure $TbFeO_3$ and g-C_3N_4 in the diffraction peaks. Also, clear peaks in the range of 27.2° were observed, which confirms the presence of g-C_3N_4. The crystal size was calculated using Scherer's equation as follows: $D = K\lambda/\beta\cos\theta$ where λ is the wavelength (Cu-K), β is the broadening of the diffraction line calculated with half maximum intensity, θ is the angle Bragg for a certain diffraction, and D_p is the crystallite size. Comparing TFCN nanocomposite (36.30 nm) with pure $TbFeO_3$ ($D_p = 34.5$ nm), the size of the TFCN nanocomposite was reduced from the

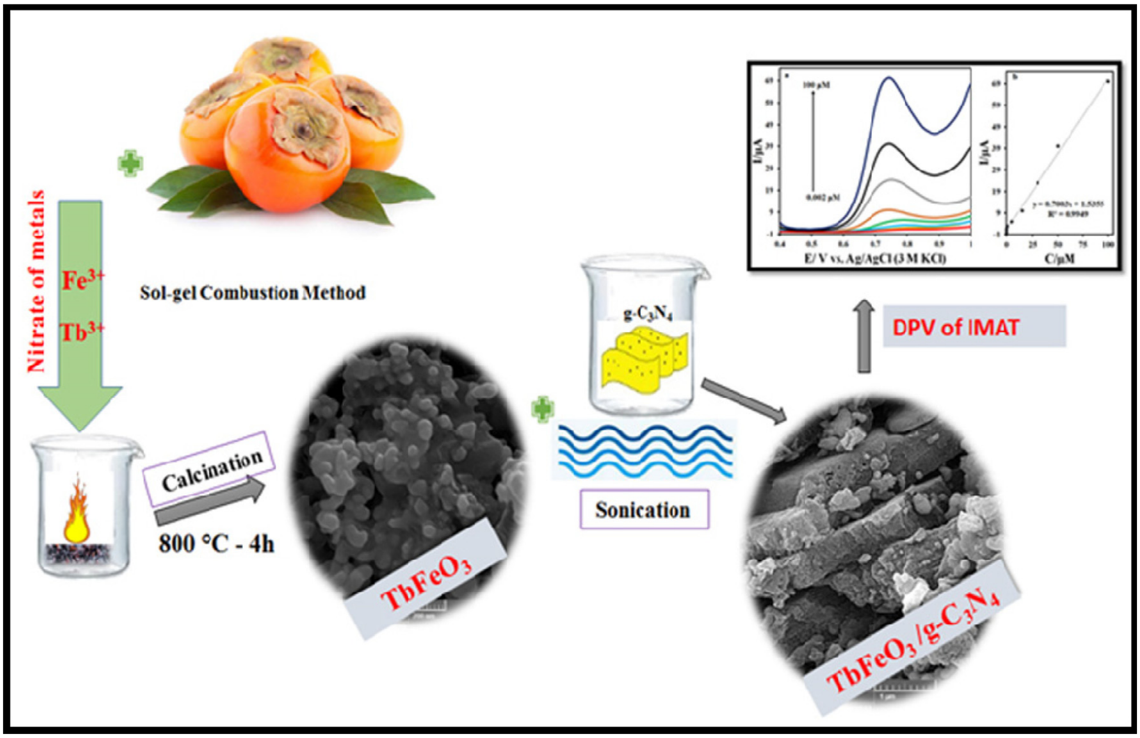

Scheme 1 The formation process of the $TbFeO_3/g\text{-}C_3N_4$ nanocomposites by sol–gel auto-combustion method using the diospyros kaki. L extract.

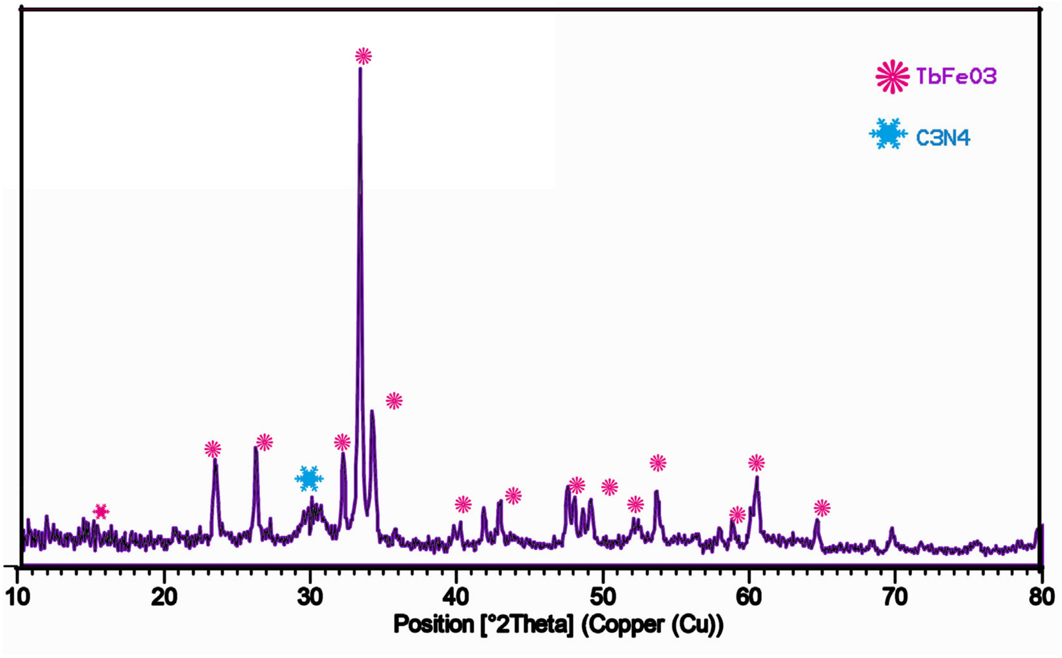

Fig. 1 XRD patterns of the $TbFeO_3/g\text{-}C_3N_4$ (1–1) nanocomposites.

sharp peak severity of the (112) plane. It is reasonable to assume that the $TbFeO_3$ particles accumulated on the surface of the $g\text{-}C_3N_4$ nanosheets are widely distributed. As a result of the above findings, it is possible to confirm the interaction between $TbFeO_3$ and $g\text{-}C_3N_4$.

3.2. FT-IR analysis

Fig. S2 (a-c) shows the Fourier transform infrared spectra of $TbFeO_3$, $g\text{-}C_3N_4$ and $TbFeO_3/g\text{-}C_3N_4$ nanocomposites. There are wide peaks at 3443 cm^{-1} and 1630 cm^{-1} in the spectra of

TFO nanoparticles and TFO/CN nanocomposites. This may be a result of the O–H stretching vibrational mode. There is also a possibility that the peaks at 439 and 565 cm^{-1} are due to Fe-O stretching vibrations (Yang et al., 2013). The calcination of the $TbFeO_3$ nanoparticles at 800 °C resulted in a weak peak at 1112 cm^{-1}, which could be caused by atmospheric carbon dioxide. It is possible to relate the absorption peak appearing at about 3200 cm^{-1} in the CN and TFO/CN spectra to the N–H bending and stretching vibrations caused by uncondensed terminal amine groups. Accordingly, direct-heated melamine products still possess amine functionalities. The typical aromatic heterocycle Graphite Carbon Nitride was found in the region between 1200 and 1650 cm^{-1}, where a number of strong peaks were observed. (Wang et al., 2017, Tian et al., 2018). As for CN, the defined peaks at 1242, 1436, and 1566 cm^{-1} corresponded to the stretching forms of the g-C_3N_4 framework structure of the conjugated aromatic ring. Graphite Carbon Nitride also exhibits a defined absorption peak at 804.94 cm^{-1} as a result of the s-triazine breathing vibration (Liu et al., 2018).

3.3. FESEM and TEM analysis

The SEM was used to examine the microscopic surface morphology of g-C_3N_4, $TbFeO_3$ and TFCN samples. Fig. S3 (a, b) shows SEM images of $TbFeO_3$ nanoparticles treated at 800 °C for 4 h with extract of Diospyros kaki. L as fuel. The results indicate that pure $TbFeO_3$ consists of large numbers of accumulated spherical nanoparticles. In Fig. S4 (a,b), SEM images are shown of well dispersed $TbFeO_3$ particles on graphite carbon nitride. Furthermore, its surface area is relatively larger. It is therefore possible to use the surface as a suitable substrate for nanoparticles.

The prepared nanocomposite was also analyzed using TEM to determine its microstructure and size. Fig. 2. For the $TbFeO_3$/g-C_3N_4 nanocomposites shown in TEM images in Fig. 2, we can clearly distinguish spherical aggregates of $TbFeO_3$ with an average diameter of about 30 nm, which is very similar to the crystallite size (D_p = 36 nm) calculated through XRD correspondence data.

3.4. EDX analysis

The Fig. S5(a,b) illustrates the elemental analysis (EDX) of synthesized TFO nanostructures and TFO/CN nanocomposites. The specific peaks of Fe, Tb, N, and O elements in Fig. S5 (b) indicate the presence of g-C_3N_4 as a substrate for $TbFeO_3$ nanostructures. EDX images confirm the stoichiometric ratio of the ingredients and the balanced dispensation of the ingredients. Furthermore, in $TbFeO_3$/g-C_3N_4 nanocomposites, the peaks clearly show the presence of C, N, Fe, and Tb elements.

3.5. VSM analysis

VSM analysis (vibrating sample magnetometer) with a topmost applied field of 1000 O_e at ambient temperature was used for studying and evaluating the magnetized properties of pure $TbFeO_3$ nanoparticles and $TbFeO_3$/g-C_3N_4 nanocomposites. In Fig. S6(a,b), we can observe the ferromagnetic behavior of both samples, with the difference that the maximum saturation magnetization (M_s) of $TbFeO_3$/g-C_3N_4 nanocomposites (0.53 emu/g) is lower than that of pure $TbFeO_3$ nanoparticles (1.51 emu/g). In contrast, the superior coercive force can maintain a substantial portion of the saturation field when the driving force is removed. In addition, a thin hysteresis loop implies a minimal amount of wasted energy. As a result, the saturated magnetic value of $TbFeO_3$ is approximately 1.51 emu/g. accordingly, the higher MS in these products is primarily attributable to the smaller particle size, as well as the greater cationic difference between the two surfaces. Due to this, we observed lower coercivity values and a special magnetic response that would probably be easily shifted and collected by an external magnetic field.

3.6. BET analysis

A survey was conducted to determine the specific surface areas of the samples and their porous structures. This was done based on nitrogen adsorption–desorption experiments at 77 K. The corresponding curves and data are shown in

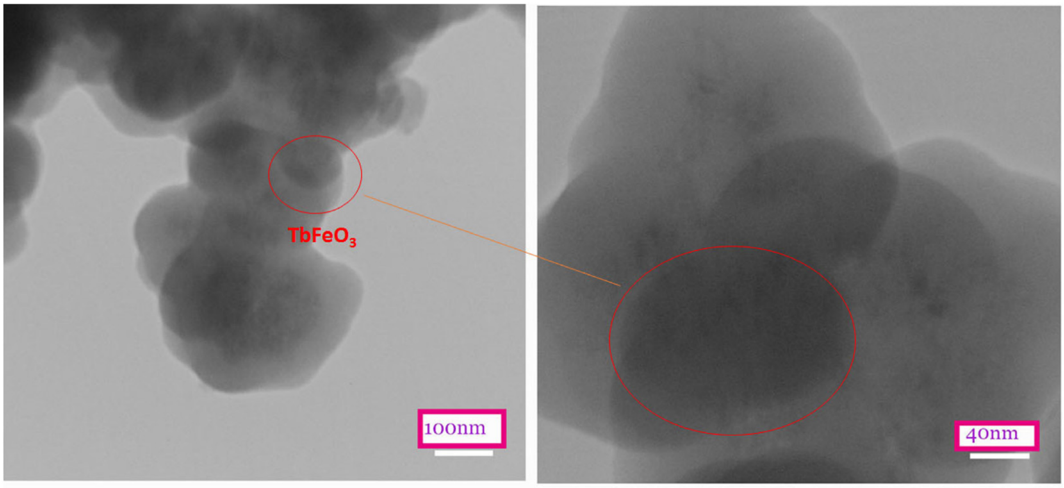

Fig. 2 TEM images of $TbFeO_3$/g-C_3N_4 (1–1) nanocomposites.

Fig. S7(a–d). These isotherms were classified as type III by the International Union of Pure and Applied Chemistry (IUPAC). The hysteresis type H_3 is associated with mesoporous and microporous materials, both of which were graded. Table.S1 shows the average diameter, total volume, and average pore diameter of nanomaterials.

3.7. *Performance of sensors*

Using the cyclic voltammetry (CV) method, the GCE, g-C_3N_4/GCE, and $TbFeO_3$/g-C_3N_4/GCE were used to investigate the electrochemical behavior of IMAT in phosphate buffer solution with pH = 7. The voltammograms obtained from the IMAT solution are shown in Fig. 3. According to the results, the oxidation current of IMAT at the surface of the unmodified electrode is 2.35 µA, while in the g-C_3N_4/GCE and $TbFeO_3$/g-C_3N_4/GCE electrodes it is 7.46 µA and 15.77 µA, respectively. Moreover, the oxidation potential of IMAT on the surfaces of GCE, g-C_3N_4/GCE, and $TbFeO_3$/C_3N_4/GCE is 0.82, 0.81, and 0.78 V, respectively, with an oxidation current starting at 0.65 V. Due to the high surface area of the electrode and the effects of carbon nitride and ferrous materials, the oxidative current of $TbFeO_3$/g-C_3N_4/GCE increases the electrode surface. In addition, these points improve the conductivity of carbon nitride and $TbFeO_3$, which results in a higher oxidation current on the surface of this electrode than on other electrodes. This may be a result of the electrostatic attraction of the analyte to the electrode surface and the existence of a large surface area for the oxidation of IMAT. Using the Randles-Sevcik equation, the surface areas of GCE, g-C3N4/GCE, and $TbFeO_3$/g-C_3N_4/GCE are 0.028, 0.037, and 0.044 cm^2, respectively.

3.8. *Optimizing modifier value*

As part of the preparation of electrochemical sensors, different quantities of nanocomposite A were investigated and IMAT was measured by cyclic voltammetry at pH = 7.0. A maximum oxidation current of IMAT was obtained using 2 µL of the synthesized nanocomposite. The oxidation current of IMAT was equal to and less than the value of 2 µL, when the amount of modifier was more than 2 µL on the surface of the electrode. In this case, the electrode surface is blocked by a higher value of the modifier, preventing IMAT penetration and reducing oxidation current. Therefore, the amount of 2 µL was selected as the optimum content (Table S2).

3.9. *pH effect*

An electrolyte solution with pH 2.0–9.0 was used to measure IMAT on the surface of $TbFeO_3$/C_3N_4/GCE.

At different pHs, no oxidation–reduction peaks related to TbFeO3/g-C3N4/GCE are observed in the electrolyte alone (Fig. 4 a). In addition, only one oxidation peak appears in the potential window of 0–1.25 V in the presence of the drug, which is related to the IMAT. CVs in Fig. 4b show the results of IMAT oxidation at pH 2.0 to 9.0 within a potential window of 0.0 to 1.25 V. The results also show that the change in pH of the electrolyte solution causes a shift in the IMAT oxidation potential, which indicates the involvement of the electrons and protons in IMAT electro-oxidation. As shown in Fig. 4c, the maximum oxidation current of IMAT at TbFeO3/C3N4/GCE was obtained at pH = 7.0, which was used as the optimal pH for other tests. The dependence of the oxidation peak potential of IMAT on pH is also shown

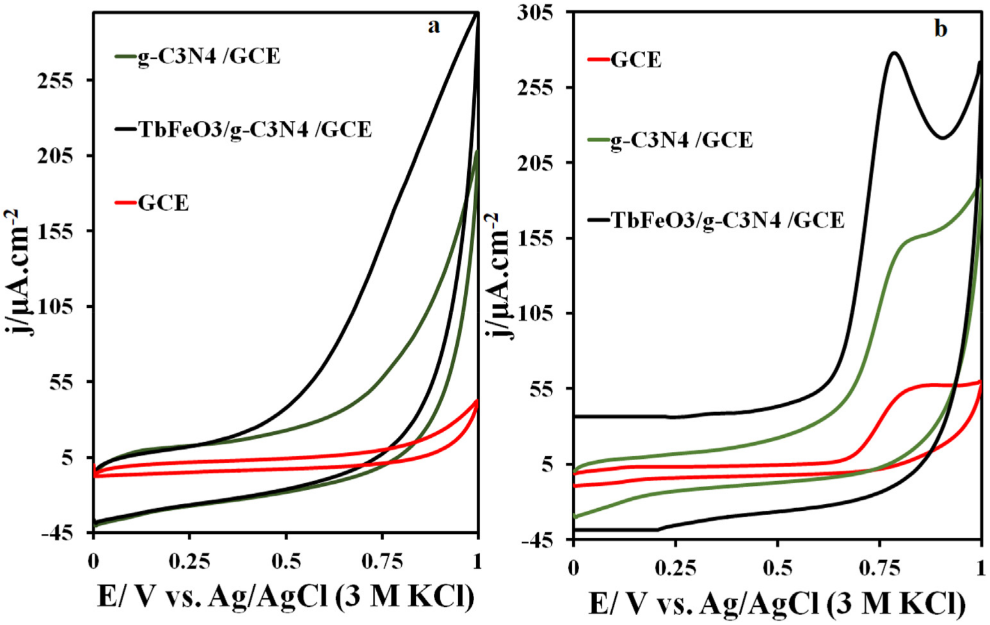

Fig. 3 CVs of GCE, g-C_3N_4/GCE, and $TbFeO_3$/g-C_3N_4/GCE surface in the presence of 5 µM IMAT and (b) the CVs on the GCE, g-C_3N_4/GCE, and $TbFeO_3$/g-C_3N_4/GCE surface in the 0.1 M phosphate buffer solution (pH = 7.0), at the scan rate of 50 mV s^{-1}, T = 25 °C.

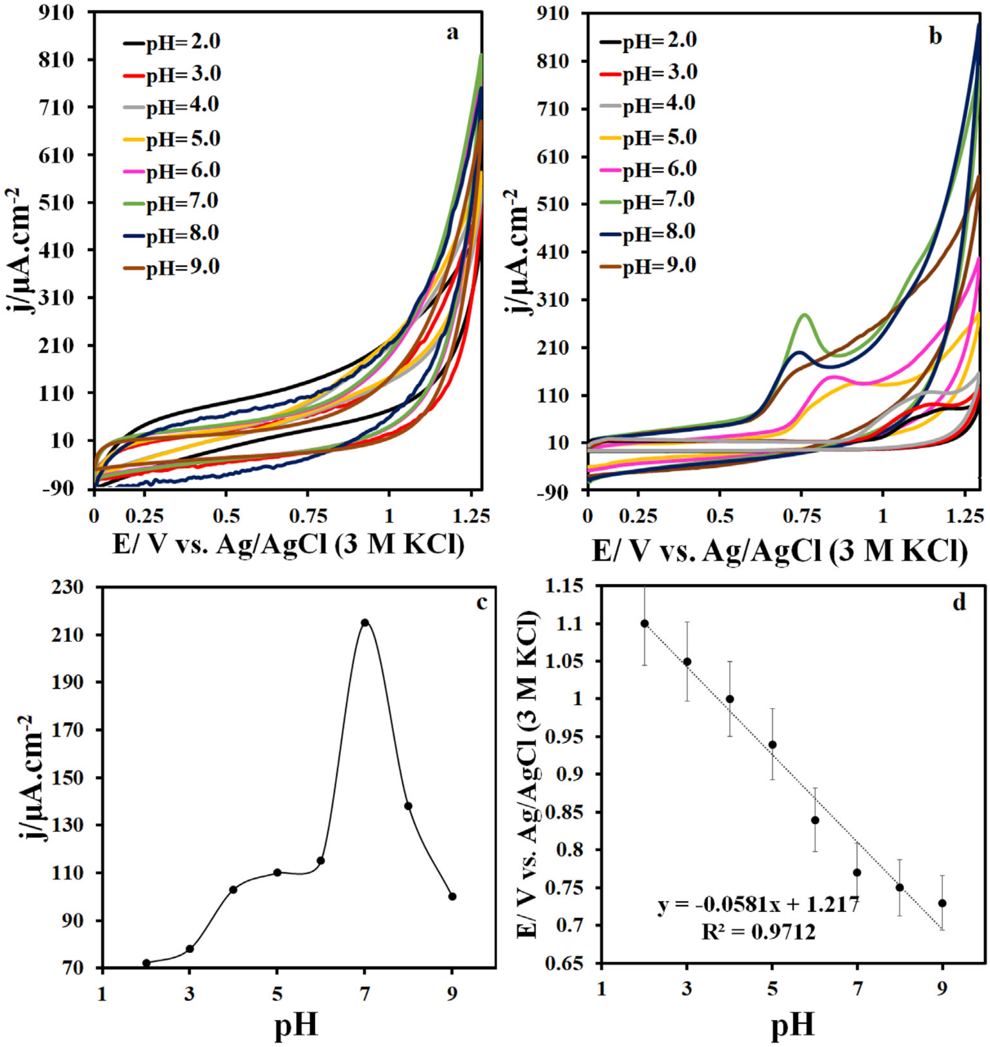

Fig. 4 (a) CVs on the $TbFeO_3/g\text{-}C_3N_4/GCE$ at various pH, (b) CVs on the $TbFeO_3/g\text{-}C_3N_4/GCE$ at various pH in the presence of 5 µM IMAT, (c) plots of the I vs. pH value and (d) I_p vs. pH value at the scan rate of 50 mV s^{-1}.

in Fig. 4d. The slope of the line obtained for this relation was 58 mV/pH, which is close to the slope of the Nernst equation. Accordingly, the number of electrons and protons participating in the oxidation of IMAT is the same.

3.10. Scan rate

On a $TbFeO_3/C_3N_4/GCE$ surface, cyclic voltammetry was used to determine scan rate during IMAT oxidation at pH = 7. The IMAT cyclic voltammograms for scan rates ranging from 10 to 300 mV/s are shown in Fig. 5a. As the scanning rate increases, oxidative current increases as well. IMAT electro-oxidation was found to be a diffusion-controlled process based on the linear increase in peak currents with the square root of the scan rate, as illustrated in Fig. 5b. Also, the potential diagram based on the logarithm of IMAT current at 10 scan rate was used in order to calculate the electron transfer coefficient. According to Equation (Slope = 2.303 RT/ (α) nF) and Fig. 5c, the electron transfer coefficient is approximately 0.61.

3.11. Analytical performance

In this study, different concentrations of IMAT were evaluated using differential pulse voltammetry (DPV) on a surface composed of $TbFeO_3/g\text{-}C_3N_4/GCE$ at pH = 7. An example of a differential pulse voltammogram for IMAT is shown in Fig. 6a. The oxidation current of IMAT also increases with an increase in IMAT concentration. Fig. 6b shows the IMAT calibration curve. For this drug, the slope of the line obtained is 0.7 µA/µM, which indicates the appropriate sensitivity of the $TbFeO_3/g\text{-}C_3N_4/GCE$ for IMAT measurements. Furthermore, the detection limit and the quantitative limit for IMAT at the $TbFeO_3/g\text{-}C_3N_4/GCE$ surface are 0.6 and 2 nM, respectively. All validation parameters were included in the calibration analysis results. There is a standard error of intercept and slope reported in the bracket in the calibration equation below (j = 5.92 (±0.004) C + 14.32 (±0.018)). Three concentrations of calibration range were examined with three replicates for intraday and interday RSD (Table S3).

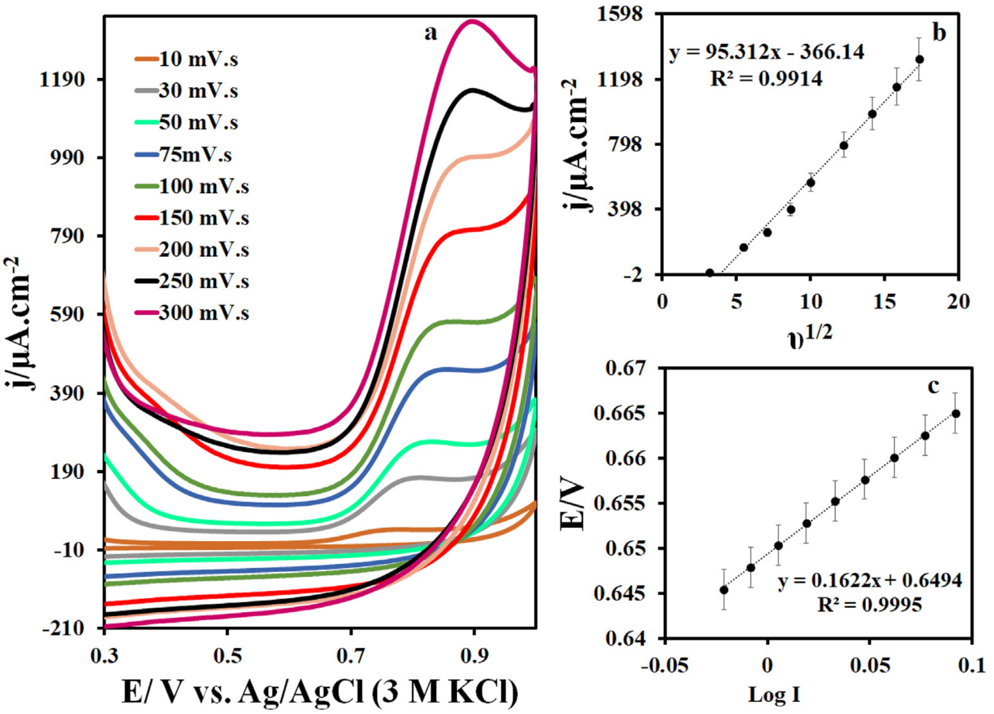

Fig. 5 (a) CVs in 0.1 M phosphate buffer solution (pH = 7.0) containing 5 µM IMAT at different scan rates (10–300 mVs^{-1}), (b) the plot of I vs. $\upsilon^{1/2}$ and (c) E vs. log I.

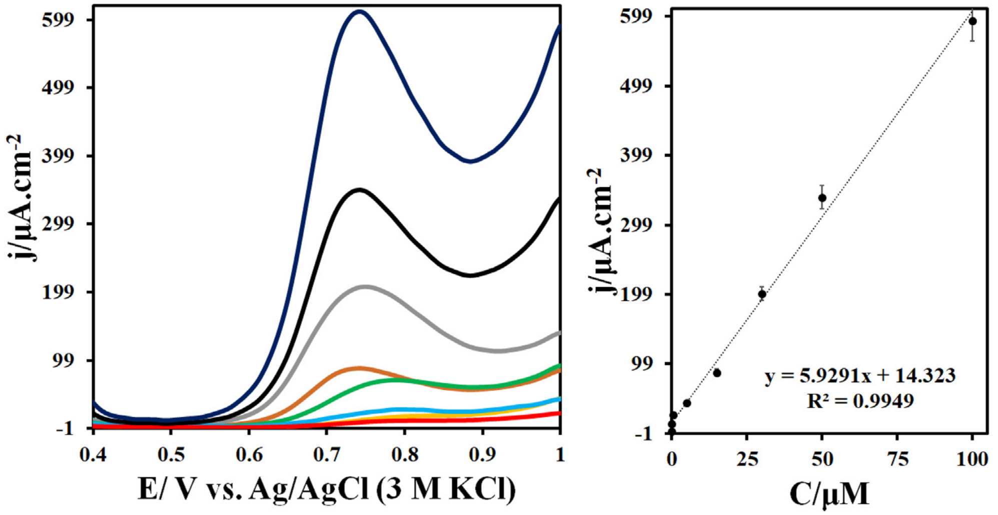

Fig. 6 (a) DPVs of $TbFeO_3$/g-C_3N_4/GCE in the presence of 0.002–100 µM IMAT in 0.1 M phosphate buffer (pH = 7.0). (b)The related linear relationships between the I and IMAT concentrations (calibration curve) in the range of 0.002 to 100 µM. (Conditions: step: 0.005 V, modulation amplitude: 0.025 V, modulation time: 0.05 s, interval time: 0.05 s and scan rate: 0.05 V/s).

The reproducibility of the GCE was determined by modifying four electrodes using $TbFeO_3$/g-C3N4/GCE and then measuring IMAT at pH = 7.0. According to the results, the standard deviation of the oxidation current of IMAT at a potential of 0.78 V is 4.63%, which indicates excellent reproducibility. IMAT measurements were conducted sequentially four times at optimum pH to investigate $TbFeO_3$/g-C_3N_4/GCE repeatability. The relative standard deviation of applied currents was found to be 3.96 percent. Based on these data, it appears that the $TbFeO_3$/g-C_3N_4/GCE has an appropriate repeatability. Five measurements were taken during a one-month period at pH = 7.0 to determine the stability of $TbFeO_3$/g-C_3N_4/GCE for IMAT measurement. In various measurements conducted over a period of one month, the oxidation current changes for IMAT were 8.38%, which indicates that the electrode is stable. We also studied the stability of the $TbFeO_3$/g-C_3N_4/GCE in 0.1 M KCl and 1 mM $K_3Fe(CN)_6$/$K_4Fe(CN)_6$ solution for 100 consecutive cycles, and the results are shown in Fig. S9. The results indicated that only 1.25% of the current of oxidation/reduction peaks decreased over 100 consecutive cycles, indicating the stability of the sensor.

In order to examine the selectivity of a drug, it must be measured concurrently with compounds present in the body or compounds that are capable of being administered simultaneously with the desired drug. There are many minerals in the body that contain Na, Ca, and Mg, or nerves that contain receptors such as dopamine (DA) and uric acid (UA); therefore, measuring the desired drug in the presence of inorganic compounds such as NaCl is essential. It has also been checked based on the sources of simultaneous prescription of IMAT and acetaminophen drugs (AC), which demonstrates the importance of simultaneous measurement. The IMAT measurements were conducted on $TbFeO_3/g\text{-}C_3N_4$/GCE surfaces containing various compounds listed in Table 1. In the presence of compounds such as dopamine, uric acid, and acetaminophen with a concentration of 150 mM, the oxidation current change for 5 mM IMAT is equal to 1.8%. Likewise, in the presence of 1 mM sodium chloride, sodium sulfate, iron chloride, copper nitrate, and calcium nitrate, the oxidation current change for IMAT is equal to $<1\%$. Among the oxidation current of IMAT, hydrogen peroxide and caffeine at a concentration of 500 mM caused the greatest change, which is equal to 1.5%. The measurement of IMAT on the surface of the electrode prepared with $TbFeO_3/g\text{-}C_3N_4$ is therefore appropriate (Fig. S10).

Table 1 Investigating the selectivity of the $TbFeO_3/g\text{-}C_3N_4$/GCE towards IMAT.

Compound	Concertation (μM)	% Changes in IMAT current
Dopamine, Uric acid and Acetaminophen	150	< 1.8 %
Sodium chloride, Sodium sulfate, Iron (II) chloride, Copper nitrate and Calcium nitrate	1000	< 1 %
Hydrogen peroxide and Caffeine	500	< 1.5%

Human blood samples were measured using the standard addition method at pH = 7 on $TbFeO_3/g\text{-}C_3N_4$/GCE surfaces. In Table 2, the concentrations of drugs added to blood samples are presented along with their standard deviations and recovery percentages. According to the results, the optimum recovery percentage in real samples is approximately 96–98, suggesting that the modified electrode is capable of measuring IMAT accurately.

Table 3 compares the performance of $TbFeO_3/g\text{-}C_3N_4$/GCE in IMAT measurement with that of other methods. Based on the results of this study, the modified electrode appears to be comparable to other methods in terms of achieving a detection limit and a wide range of concentrations. The modified electrode was prepared by a simple and cost-effective procedure that is more readily available than materials used in other electrochemical methods. As a result, the modified electrode used in this study is desirable in terms of its detection limit and wide range of concentrations.

4. Conclusion

In this study, $TbFeO_3/g\text{-}C_3N4$ was placed on the surface of a GCE to measure IMAT using differential and cyclic pulse voltammetry. By combining $TbFeO_3/g\text{-}C_3N_4$, an excellent nanocomposite was created with a high surface area and good conductivity, which led to satisfac-

Table 2 IMAT determination in plasma sample using a $TbFeO_3/g\text{-}C_3N_4$/GCE.

Sample	Added (μM)	Found (μM)	Recovery (%) (n = 3)	RSD%
Plasma	0	–	–	–
	0.50	0.48	96.00	5.33
	5.00	4.86	97.20	4.83
	15.00	14.76	98.40	4.70

Table 3 Comparison of the analytical parameters of diverse sensors in IMAT sensing.

Sensor	Method	Linear range (μM)	LOD (nM)	Synthesis method	Ref.
Dendrimer/PEG	DPV	0.01–200	7.3	expensive	(Hatamluyi and Es' haghi 2017)
MWCNT/SPCE	SWV	0.005–0.912	7.0	Time-consuming, expensive	(Rodríguez et al., 2018)
MWCNT/NiO-ZnO/GCE	DPV	0.015–2	2.4	expensive, Fairly hard	(Chen et al., 2019)
Cu-BTC/RGO/GCE	DPV	0.04–80	6.0	Time-consuming, expensive	(Rezvani Jalal et al., 2020)
Fe_3O_4@MWCNTs@PANNFs/CPE	DPV	0.001–0.85	0.4	Time-consuming, expensive and Fairly hard	(Ghapanvari et al., 2020)
RGO/AgNPs/GCE	DPV	0.001–280	1.1	Time-consuming, expensive	(Wu et al., 2021)
Cu-BTC/MWCNT/GCE	DPV	0.01–220	4.1	Fairly hard, expensive	(Pour et al., 2021)
$TbFeO_3/g\text{-}C_3N_4$/GCE	DPV	0.002–100	0.6	Very Simple, affordable	This work

tory results in the IMAT tests. Due to the increased electron transfer rate at the surface of the $TbFeO_3$/g-C_3N_4/GCE electrode at pH = 7.0, the oxidation current of IMAT was higher than the oxidation current of the other electrodes. The excellent results are attributed to the large electrode surface area provided by g-C_3N_4 and $TbFeO_3$, as well as their excellent catalytic properties. Thus, these electrodes can be used as electrochemical sensors based on their performance. IMAT showed a linear detection limit of 0.002–100 µM equal to 0.6 nM. One of the most important outcomes of the electrochemical sensor prepared for IMAT is its excellent detection limit in comparison to other methods. Besides its special selectivity, repeatability, and stability, this sensor showed beneficial results in measuring IMAT in real samples.

CRediT authorship contribution statement

Mahin Baladi: Investigation, Formal analysis, Methodology, Software, Writing – review & editing, Writing – original draft. **Hakimeh Teymourinia:** Investigation, Writing – review & editing, Software, Formal analysis, Methodology, Writing – original draft, Software. **Elmuez A. Dawi:** Software, Writing – review & editing, Visualization. **Mahnaz Amiri:** Supervision, Software, Data curation, Validation, Resources. **Ali Ramazani:** Software, Data curation, Validation, Resources. **Masoud Salavati-Niasari:** Software, Formal analysis, Methodology, Writing – review & editing, Writing – original draft, Conceptualization, Supervision, Project administration, Investigation, Data curation, Validation, Resources, Visualization, Funding acquisition.

Declaration of Competing Interest

The authors declare that they have no known competing financial interests or personal relationships that could have appeared to influence the work reported in this paper.

Appendix A. Supplementary data

Supplementary data to this article can be found online at https://doi.org/10.1016/j.arabjc.2023.104963.

References

Abbasi, M., Alsaikhan, F., Obaid, R.F., et al, 2023. Development of the DNA-based voltammetric biosensor for detection of vincristine as anticancer drug. Front. Chem. 2023 (10), 1060706. https://doi.org/10.3389/fchem.2022.1060706.

Abdulhusain, Z.H., Mahdi, M.A., Abdulsahib, W.K., Jasim, L.S., 2022. Anabasis articulata exerts an anti-arthritic effect on adjuvant-induced arthritis in rats. J. Adv. Pharm. Technol. Res. 13 (4), 276–280. https://doi.org/10.4103/japtr.japtr_440_22.

Ajimura, T.O., Borges, K.B., Ferreira, A.F., et al, 2011. Capillary electrophoresis method for plasmatic determination of imatinib mesylate in chronic myeloid leukemia patients. Electrophoresis 32, 1885–1892.

Al-Alwany, A.A., 2022. Arrhythmia related to hypertensive left ventricular hypertrophy in Iraqi patients: frequency and outcome. J. Med. Life 15 (9), 1115. https://doi.org/10.25122/jml-2022-0214.

Amiri, M., Mahmoudi-Moghaddam, H., 2021. Green synthesis of ZnO/ZnCo2O4 and its application for electrochemical determination of bisphenol A. Microchem. J. 160, 105663.

Anajafi, Z., Naseri, M., Marini, S., et al, 2019. NdFeO3 as a new electrocatalytic material for the electrochemical monitoring of dopamine. Anal. Bioanal. Chem. 411, 7681–7688.

Andriamanana, I., Gana, I., Duretz, B., et al, 2013. Simultaneous analysis of anticancer agents bortezomib, imatinib, nilotinib, dasatinib, erlotinib, lapatinib, sorafenib, sunitinib and vandetanib in human plasma using LC/MS/MS. J. Chromatogr. B 926, 83–91.

Atta, N.F., El-Ads, E.H., Galal, A., et al, 2019. Electrochemical sensing platform based on nano-perovskite/glycine/carbon composite for amlodipine and ascorbic acid drugs. Electroanalysis 31, 448–460.

Bobinov, V., Goroshchenko, S., Rozhchenko, L., Samochernykh, K., Petrov, A., 2021. Historical aspects of microsurgical treatment of brain aneurysms. Hist. Med. 7 (2), 179–188. https://doi.org/10.17720/2409-5834.v7.2.2021.08h.

Chen, H., Luo, K., Li, K., 2019. A facile electrochemical sensor based on NiO-ZnO/MWCNT-COOH modified GCE for simultaneous quantification of imatinib and itraconazole. J. Electrochem. Soc. 166, B697.

Deininger, M.W., Druker, B.J., 2003. Specific targeted therapy of chronic myelogenous leukemia with imatinib. Pharmacol. Rev. 55, 401–423.

Druker, B.J., Sawyers, C.L., Kantarjian, H., et al, 2001. Activity of a specific inhibitor of the BCR-ABL tyrosine kinase in the blast crisis of chronic myeloid leukemia and acute lymphoblastic leukemia with the Philadelphia chromosome. N. Engl. J. Med. 344, 1038–1042.

Farvardin, N., Jahani, S., Kazemipour, M., et al, 2020. The synthesis and characterization of 3D mesoporous CeO 2 hollow spheres as a modifier for the simultaneous determination of amlodipine, hydrochlorothiazide and valsartan. Anal. Methods 12, 1767–1778.

Foroughi, M.M., Jahani, S., 2022. Investigation of a high-sensitive electrochemical DNA biosensor for determination of Idarubicin and studies of DNA-binding properties. Microchem. J. 179, 107546.

Ghalkhani, M., Gharagozlou, M., Sohouli, E., et al, 2022. Preparation of an electrochemical sensor based on a HKUST-1/CoFe2O4/SiO2-modified carbon paste electrode for determination of Azaperone. Microchem. J. 107199.

Ghapanvari, M., Madrakian, T., Afkhami, A., et al, 2020. A modified carbon paste electrode based on Fe 3 O 4@ multi-walled carbon nanotubes@ polyacrylonitrile nanofibers for determination of imatinib anticancer drug. J. Appl. Electrochem. 50, 281–294.

Ghasemi, L., Jahani, S., Ghazizadeh, M., et al, 2023. Simultaneous determination of amitriptyline and venlafaxine using a novel voltammetric sensor of carbon paste electrode modified with octahedral Pd2+-doped Co3O4 composite. Mater. Chem. Phys. 296, 127176.

Gibbons, J., Egorin, M.J., Ramanathan, R.K., et al, 2008. Phase I and pharmacokinetic study of imatinib mesylate in patients with advanced malignancies and varying degrees of renal dysfunction: a study by the National Cancer Institute Organ Dysfunction Working Group. J. Clin. Oncol. 26, 570–576.

Gondo, H.K., 2022. Effect of Isotiocyanate Therapy on trophoblast cell culture hyperglycemia atmosphere in apoptosis, caspase-3, NO, VEGF. Hist. Med. 8 (1), 62–67. https://doi.org/10.17720/2409-5834.v8.1.2022.008.

Halali, V.V., Sanjayan, C., Suvina, V., et al, 2020. Perovskite nanomaterials as optical and electrochemical sensors. Inorg. Chem. Front. 7, 2702–2725.

Hasin, F., Islam, M., Ahmad, M., et al, 2017. Validation of assay method for the estimation of imatinib mesylate in tablet dosage form by HPLC. Eur. J. Biomed. Pharm. Sci.

Hassannezhad, M., Hosseini, M., Ganjali, M.R., et al, 2019. A graphitic carbon nitride (gC 3 N 4/Fe 3 O 4) nanocomposite: an efficient electrode material for the electrochemical determination of tramadol in human biological fluids. Anal. Methods 11, 2064–2071.

Hatamluyi, B., Es' haghi, Z., 2017. A layer-by-layer sensing architecture based on dendrimer and ionic liquid supported reduced graphene oxide for simultaneous hollow-fiber solid phase microextraction and electrochemical determination of anti-cancer drug imatinib in biological samples. J. Electroanal. Chem. 801, 439–449.

Hunter, T., 2007. Treatment for chronic myelogenous leukemia: the long road to imatinib. J. Clin. Invest. 117, 2036–2043.

Iranmanesh, T., Jahani, S., Foroughi, M.M., et al, 2020. Synthesis of La 2 O 3/MWCNT nanocomposite as the sensing element for electrochemical determination of theophylline. Anal. Methods 12, 4319–4326.

Jahani, S., Sedighi, A., Toolabi, A., et al, 2022. Development and characterization of La2O3 nanoparticles@ snowflake-like Cu2S nanostructure composite modified electrode and application for simultaneous detection of catechol, hydroquinone and resorcinol as an electrochemical sensor. Electrochim. Acta 416, 140261.

Karim, S.E.A., El-Nashar, R.M., Abadi, A.H., 2012. Potentiometric determination of imatinib under batch and flow injection analysis conditions. Int. J. Electrochem. Sci. 7, 9668–9681.

Karim, S.S.E.A., Farghaly, R.A., El-Nashar, R.M., et al, 2014. Spectrophotometric determination of imatinib mesylate using charge transfer complexes in pure form and pharmaceutical formulation. Chem. Rapid Commun. 2, 55–63.

Larson, R.A., Druker, B.J., Guilhot, F., et al, 2008. Imatinib pharmacokinetics and its correlation with response and safety in chronic-phase chronic myeloid leukemia: a subanalysis of the IRIS study. Blood, J. Am. Soc. Hematol. 111, 4022–4028.

Liu, E., Jin, C., Xu, C., et al, 2018. Facile strategy to fabricate Ni2P/g-C3N4 heterojunction with excellent photocatalytic hydrogen evolution activity. Int. J. Hydrogen Energy 43, 21355–21364.

Mahde, B.W., Sultan, A.M., Mahdi, M.A., Jasim, L.S., 2022. Kinetic adsorption and release study of sulfadiazine hydrochloride drug from aqueous solutions on GO/P(AA-AM-MCC) composite. Int. J. Drug Del. Technol. 12 (4), 1583–1589. https://doi.org/10.25258/ijddt.12.4.17.

Matheus, J.R.V., Andrade, C.J.D., Miyahira, R.F., et al, 2022. Persimmon (Diospyros kaki L.): Chemical properties, bioactive compounds and potential use in the development of new products–A review. Food Rev. Intl. 38, 384–401.

Mauro, M.J., Deininger, M., 2006. Chronic myeloid leukemia in 2006: a perspective. Haematologica 91, 152.

Moarefdoust, M.M., Jahani, S., Moradalizadeh, M., et al, 2021. An electrochemical sensor based on hierarchical nickel oxide nanostructures doped with indium ions for voltammetric simultaneous determination of sunset yellow and tartrazine colorants in soft drink powders. Anal. Methods 13, 2396–2404.

Mohaghegh, S., Tarighatnia, A., Omidi, Y., et al, 2022. Multifunctional magnetic nanoparticles for MRI-guided co-delivery of erlotinib and L-asparaginase to ovarian cancer. J. Microencapsul. 39, 394–408.

Nabi, P.N., Vahidfar, N., Tohidkia, M.R., et al, 2021. Mucin-1 conjugated polyamidoamine-based nanoparticles for image-guided delivery of gefitinib to breast cancer. Int. J. Biol. Macromol. 174, 185–197.

Pour, B.H., Haghnazari, N., Keshavarzi, F., et al, 2021. High sensitive electrochemical sensor for imatinib based on metal-organic frameworks and multiwall carbon nanotubes nanocomposite. Microchem. J. 165, 106147.

Rahimi Kakavandi, N., Asadi, T., Jannat, B., et al, 2021. Method development for determination of imatinib and its major metabolite, N-desmethyl imatinib, in biological and environmental samples by SA–SHS–LPME and HPLC. Biomed. Chromatogr. 35, e5088.

Rezvani Jalal, N., Madrakian, T., Afkhami, A., et al, 2020. In situ growth of metal–organic framework HKUST-1 on graphene oxide nanoribbons with high electrochemical sensing performance in imatinib determination. ACS Appl. Mater. Interfaces 12, 4859–4869.

Rodriguez, J., Berzas, J., Castaneda, G., et al, 2005. Voltammetric determination of Imatinib (Gleevec) and its main metabolite using square-wave and adsorptive stripping square-wave techniques in urine samples. Talanta 66, 202–209.

Rodríguez, J., Castañeda, G., Lizcano, I., 2018. Electrochemical sensor for leukemia drug imatinib determination in urine by adsorptive striping square wave voltammetry using modified screen-printed electrodes. Electrochim. Acta 269, 668–675.

Rodríguez-Flores, J., Nevado, J.B., Salcedo, A.C., et al, 2005. Nonaqueous capillary electrophoresis method for the analysis of gleevec and its main metabolite in human urine. J. Chromatogr. A 1068, 175–182.

Salavati-Niasari, M., Amiri, A., 2005. Synthesis and characterization of alumina-supported Mn(II), Co(II), Ni(II) and Cu(II) complexes of bis (salicylaldiminato) hydrazone as catalysts for oxidation of. Appl. Catal. A 290 (1–2), 46–53. https://doi.org/10.1016/j.apcata.2005.05.009.

Salavati-Niasari, M., Hasanalian, J., Najafian, H., 2004. Alumina-supported FeCl3, MnCl2, CoCl2, NiCl2, CuCl2, and ZnCl2 as catalysts for the benzylation of benzene by benzyl chloride. J. Mol. Catal. A Chem. 209 (1–2), 209–214. https://doi.org/10.1016/j.molcata.2003.08.027.

Salavati-Niasari, M., Davar, F., Fereshteh, Z., 2009. Synthesis and characterization of ZnO nanocrystals from thermolysis of new precursor. Chem. Eng. J. 146 (3), 498–502. https://doi.org/10.1016/j.cej.2008.09.042.

Sohouli, E., Adib, K., Maddah, B., et al, 2022. Preparation of a supercapacitor electrode based on carbon nano-onions/manganese dioxide/iron oxide nanocomposite. J. Storage Mater. 52, 104987.

Sohouli, E., Adib, K., Maddah, B., et al, 2022. Manganese dioxide/cobalt tungstate/nitrogen-doped carbon nano-onions nanocomposite as new supercapacitor electrode. Ceram. Int. 48, 295–303.

Taherizadeh, M., Jahani, S., Moradalizadeh, M., et al, 2023. Synthesis of a dual-functional terbium doped copper oxide nanoflowers for high-efficiently electrochemical sensing of ofloxacin, pefloxacin and gatifloxacin. Talanta 255, 124216.

Tajik, S., Orooji, Y., Ghazanfari, Z., et al, 2021. Nanomaterials modified electrodes for electrochemical detection of Sudan I in food. J. Food Meas. Charact. 15, 3837–3852.

Terán-Alcocer, Á., Bravo-Plascencia, F., Cevallos-Morillo, C., et al, 2021. Electrochemical sensors based on conducting polymers for the aqueous detection of biologically relevant molecules. Nanomaterials 11, 252.

Teymourinia, H., Darvishnejad, M.H., Amiri, O., et al, 2020. GQDs/Sb2S3/TiO2 as a co-sensitized in DSSs: improve the power conversion efficiency of DSSs through increasing light harvesting by using as-synthesized nanocomposite and mirror. Appl. Surf. Sci. 512, 145638.

Tian, J., Zhang, L., Wang, M., et al, 2018. Remarkably enhanced H2 evolution activity of oxidized graphitic carbon nitride by an extremely facile K2CO3-activation approach. Appl. Catal. B 232, 322–329.

Vijayaraghavan, T., Sivasubramanian, R., Hussain, S., et al, 2017. A facile synthesis of LaFeO3-based perovskites and their application towards sensing of neurotransmitters. ChemistrySelect 2, 5570–5577.

Wang, W., An, T., Li, G., et al, 2017. Earth-abundant Ni2P/g-C3N4 lamellar nanohydrids for enhanced photocatalytic hydrogen evolution and bacterial inactivation under visible light irradiation. Appl. Catal. B 217, 570–580.

Wang, Z.-W., Liu, H.-J., Li, C.-Y., et al, 2020. Mesoporous g-C3N4/β-CD nanocomposites modified glassy carbon electrode for electrochemical determination of 2, 4, 6-trinitrotoluene. Talanta 208, 120410.

Warshi, M.K., Mishra, V., Sagdeo, A., et al, 2018. Structural, optical and electronic properties of RFeO3. Ceram. Int. 44, 8344–8349.

Wu, Z., Liu, J., Liang, M., et al, 2021. Detection of imatinib based on electrochemical sensor constructed using biosynthesized graphene-silver nanocomposite. Front. Chem. 9, 670074.

Yang, H., Zhang, J., Lin, G., et al, 2013. Preparation, characterization and photocatalytic properties of terbium orthoferrite nanopowder. Adv. Powder Technol. 24, 242–245.

Yousefi, M., Gholamian, F., Ghanbari, D., Salavati-Niasari, M., 2011. Polymeric nanocomposite materials: preparation and characterization of star-shaped PbS nanocrystals and their influence on the thermal stability of acrylonitrile–butadiene. Polyhedron 30 (6), 1055–1060. https://doi.org/10.1016/j.poly.2011.01.012.

Zhang, L., Liu, C., Wang, Q., et al, 2020. Electrochemical sensor based on an electrode modified with porous graphitic carbon nitride nanosheets (C3N4) embedded in graphene oxide for simultaneous determination of ascorbic acid, dopamine and uric acid. Microchim. Acta 187, 1–10.

Zhang, H., Yi, J., Jiang, X., 2017. Fast response, highly sensitive and selective mixed-potential H2 sensor based on (La, Sr)(Cr, Fe) O3-δ perovskite sensing electrode. ACS Appl. Mater. Interfaces 9, 17218–17225.